



The Discovery of Polarized Water Vapor Megamaser Emission in a Molecular Accretion Disk

Downloaded from: <https://research.chalmers.se>, 2024-11-19 09:17 UTC







Citation for the original published paper (version of record):

Gallimore, J., Impellizzeri, C., Aghelpasand, S. et al (2024). The Discovery of Polarized Water Vapor Megamaser Emission in a Molecular Accretion Disk. *Astrophysical Journal Letters*, 975(1).
<http://dx.doi.org/10.3847/2041-8213/ad864f>

N.B. When citing this work, cite the original published paper.



The Discovery of Polarized Water Vapor Megamaser Emission in a Molecular Accretion Disk

Jack F. Gallimore¹ , C. M. Violette Impellizzeri^{2,3} , Samaneh Aghelpasand⁴ , Feng Gao⁵ , Virginia Hostetter¹ , and Boy Lankhaar^{3,6} 

¹ Department of Physics and Astronomy, Bucknell University, Lewisburg, PA 17837, USA; jgallimo@bucknell.edu

² Institute ASTRON, Netherlands Institute for Radio Astronomy, NL-7991 PD Dwingeloo, The Netherlands

³ Leiden Observatory, Leiden University, P.O. Box 9513, 2300 RA, Leiden, The Netherlands

⁴ Department of Physics, Alzahra University, North Sheikh Bahae St., Deh-e-Vanak, Tehran, 19938-91176, Iran

⁵ Max-Planck-Institut für Radioastronomie, Auf dem Hügel 69, 53121 Bonn, Germany

⁶ Department of Space, Earth and Environment, Chalmers University of Technology, Onsala Space Observatory, 439 92, Onsala, Sweden

Received 2024 September 19; revised 2024 October 10; accepted 2024 October 14; published 2024 October 25

Abstract

For the first time in an extragalactic source, we detect linearly polarized H₂O maser emission associated with the molecular accretion disk of NGC 1068. The position angles of the electric polarization vectors are perpendicular to the axes of filamentary structures in the molecular accretion disk. The inferred magnetic field threading the molecular disk must lie within $\sim 35^\circ$ of the sky plane. The orientation of the magnetic fields relative to the disk plane implies that the maser region is unstable to hydromagnetically powered outflow; we speculate that the maser region may be the source of the larger-scale molecular outflow found in Atacama Large Millimeter/submillimeter Array studies. The new very long baseline interferometry observations also reveal a compact radio continuum source, NGC 1068*, aligned with the near-systemic maser spots. The molecular accretion disk must be viewed nearly edge on, and the revised central mass is $M = (16.6 \pm 0.1) \times 10^6 M_\odot$.

Unified Astronomy Thesaurus concepts: [Megamasers \(1023\)](#); [Water masers \(1790\)](#); [Supermassive black holes \(1663\)](#); [Seyfert galaxies \(1447\)](#); [Accretion \(14\)](#); [Very long baseline interferometry \(1769\)](#); [Active galactic nuclei \(16\)](#)

1. Introduction

Extragalactic H₂O masers, or megamasers, are usually associated with (sub)parsec-scale, edge-on molecular accretion disks, jet-induced shocks, or molecular outflows in narrow-line active galaxies (K. Y. Lo 2005). Famously, where they occur in disks, their distances can be determined geometrically through kinematic parallax (e.g., J. R. Herrnstein et al. 1999; E. M. L. Humphreys et al. 2013; F. Gao et al. 2016). Disk megamasers commonly show a Keplerian rotation curve, precisely measuring the central compact mass, presumably a supermassive black hole (SMBH; e.g., C. Y. Kuo et al. 2011; F. Gao et al. 2017).

In various models for accretion disks, the magnetic field plays an important role, ultimately providing an effective viscosity that drives accretion (D. M. Eardley & A. P. Lightman 1975; S. A. Balbus & J. F. Hawley 1998; M. A. Abramowicz & P. C. Fragile 2013). Ordered and inclined magnetic fields can accelerate clouds, generate outflow, and remove angular momentum from the accretion disk (R. D. Blandford & D. G. Payne 1982; R. T. Emmering et al. 1992). M. Elitzur & I. Shlosman (2006) proposed that the resulting molecular outflow might provide the torus scale height requisite for obscuration-based unification schemes for active galactic nuclei (see R. Antonucci 1993; C. Ramos Almeida & C. Ricci 2017, for reviews of such unification schemes). As such, measuring the strength and orientation of the magnetic fields in accretion disks contributes to our understanding of the accretion process.

Linear and circular polarization of maser emission measure the magnetic field strength and orientation in molecular gas (P. Goldreich et al. 1973). Since H₂O is a nonparamagnetic molecule, its Zeeman splitting in mG magnetic fields is insufficient to produce detectable circular polarization, even in very narrow maser lines (S. Deguchi & W. D. Watson 1986; B. Lankhaar & R. Teague 2023). Despite several attempts (e.g., J. R. Herrnstein et al. 1998; M. Modjaz et al. 2005; G. Surcis et al. 2020), H₂O megamaser circular polarization observations have only yielded upper limits to the line-of-sight component of the magnetic field, with the most stringent limit being $B_{\text{los}} < 11$ mG toward NGC 3079 (W. H. T. Vlemmings et al. 2007). Linear polarization of masers is more complicated and depends on the saturation degree, anisotropy of the pumping mechanism, and propagation angle relative to the magnetic field axis, θ (see, e.g., the discussion in S. Deguchi et al. 1995). As long as the magnetic precession rate ($\sim 1 \text{ s}^{-1} \text{ mG}^{-1}$ for the H₂O 22 GHz transition) exceeds the rate of stimulated emission, then the electric polarization vector aligns parallel or perpendicular to the projection of the magnetic field on the sky (P. Goldreich & N. D. Kylafis 1981): when $\theta \lesssim 55^\circ$, the polarization vector aligns with the projected magnetic field direction; otherwise, the polarization is perpendicular to the magnetic field (see the discussion in W. H. T. Vlemmings et al. 2006). B. Lankhaar et al. (2024) demonstrated that anisotropically pumped 22 GHz H₂O masers should show 1%–3% linear polarization below the saturation limit, i.e., the limit at which stimulated emission exceeds the decay rate; isotropic pumping produces significant linear polarization only above the saturation limit. Unlike circular polarization, the linear



Original content from this work may be used under the terms of the [Creative Commons Attribution 4.0 licence](#). Any further distribution of this work must maintain attribution to the author(s) and the title of the work, journal citation and DOI.

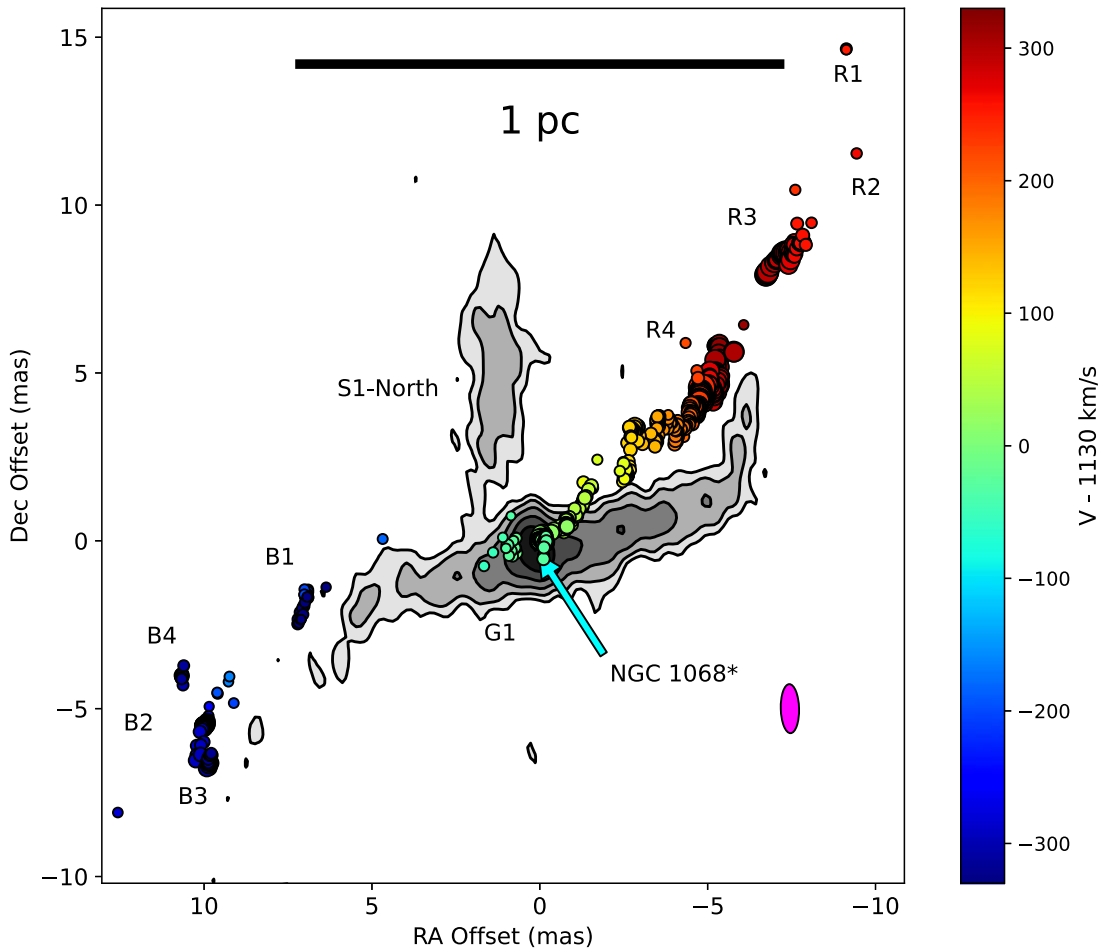


Figure 1. An overlay of H_2O maser spot positions and the 21.9 GHz continuum image of the radio component S1 of NGC 1068. Coordinate offsets are relative to R. A. (J2000) = $02^{\text{h}}42^{\text{m}}40^{\text{s}}.70907$, decl. (J2000) = $-00^{\circ}00'47''.9444$. Maser spots are plotted as filled circles color coded to the recessional velocity relative to V (LSRK) = 1130 km s^{-1} . The size of the maser spots scales with the square root of the integrated flux density (i.e., larger circles are brighter maser spots). The brightest maser groups (R1, R2, etc.) are labeled using the naming convention of [GI23](#). The radio continuum is plotted as filled contours. The contour levels are -34 (dashed), 34 , 57 , 97 , 164 , and $276 \mu\text{Jy beam}^{-1}$. The equivalent brightness temperatures are $(-0.11, 0.11, 0.18, 0.31, 0.53, 0.88) \times 10^6 \text{ K}$. The peak surface brightness is $451.5 \pm 0.1 \mu\text{Jy beam}^{-1}$, equivalent to brightness temperature $(1.45 \pm 0.05) \times 10^6 \text{ K}$. The locations of the central compact continuum source, NGC 1068*, and the northern continuum plume, S1-North, are annotated. The continuum restoring beam (FWHM) is the magenta ellipse at the lower right.

polarization fraction of H_2O masers does not directly constrain the strength of the magnetic field.

The Seyfert 2 galaxy NGC 1068 is an unusual H_2O megamaser source. The brightest masers are found in a molecular accretion disk surrounding the central engine, radio continuum source S1 (J. F. Gallimore et al. 1996, 2001). To orient the reader, Figure 1 shows the sky distribution of the disk maser spots relative to radio continuum. The position–velocity diagram, taken along the major axis position angle ($\text{PA} = -50^\circ$), suggests a rotation curve slightly flatter than Keplerian rotation (L. J. Greenhill & C. R. Gwinn 1997). However, J. F. Gallimore & C. M. V. Impellizzeri (2023; hereafter [GI23](#)) demonstrated that the apparently too flat rotation curve may be an illusion that results from how the water masers preferentially sample spiral arms within the disk; the fully three-dimensional model is consistent with Keplerian rotation around a $17 \times 10^6 M_\odot$ SMBH.

The maser disk also shows filamentary substructures; these filaments are especially prominent in the brightest masers, the R4 group. Since the maser region is expected to be partially ionized (D. A. Neufeld et al. 1994; D. A. Neufeld & P. R. Maloney 1995), the filaments suggest organization by an orderly magnetic field threading the disk ([GI23](#)). The filament lengths are typically

1–2 mas or roughly 0.1 pc at the distance of NGC 1068.⁷ [GI23](#) estimated that the magnetic field strengths must be $B \gtrsim 2 \text{ mG}$ to remain orderly in the presence of turbulent motions in the molecular gas. This estimate compares well with an independent measurement from infrared polarimetry, $B \gtrsim 4 \text{ mG}$ (E. Lopez-Rodriguez et al. 2015).

We obtained new observations of the 22 GHz H_2O megamasers of NGC 1068 to search for polarization as a tool to map the magnetic fields in the molecular accretion disk. As a by-product, we obtained sensitive, wideband continuum measurements that provide the currently highest-resolution map of the radio continuum source. Below, we discuss the observations and data reduction, the primary findings, and summarize our main conclusions.

2. Observations and Data Reduction

We observed NGC 1068 with the High Sensitivity Array (HSA), consisting of the 10 VLBA telescopes augmented by

⁷ The distance to NGC 1068 is $13.97 \pm 2.1 \text{ Mpc}$ (G. S. Anand et al. 2021). We adopt the scale $1'' = 70 \text{ pc}$, appropriate for a distance of 14.4 Mpc, to maintain consistency with previous work.

the Green Bank Telescope (GBT) and the Karl G. Jansky Very Large Array (VLA) acting as a phased telescope. The observations took place on 2021 November 14, starting at UTC 03:36 and lasting six hours. The receivers were tuned to four intermediate frequency bands (IFs) centered at 21.776, 21.904, 22.032, and 22.160 GHz; the three lower-frequency IFs cover the continuum well separated from the H₂O line, and the high-frequency IF centers near the water maser transition $\nu_0 = 22.23508$ GHz, redshifted to V (LSRK) = 1130 km s⁻¹. Observations were performed with full polarization, permitting measurements in parallel-hand circular polarization (right-hand RR and left-hand LL) to produce images in Stokes I and V and cross-hand polarization (RL and LR) to produce images in Stokes Q and U .

2.1. Data Reduction

Roughly half of the observing time was dedicated to NGC 1068, with short gaps for observations of calibrator sources. Every five minutes, the calibrator J0238+16 was observed to align the phases of the VLA antennas. The phase reference calibrator J0239–02 was observed for three minutes every half hour to monitor instrumental delays and as an astrometric reference. We also observed the bright radio source 3C 454.3 to calibrate bandpass and multiband delays, 3C 84 as a low-polarization reference to remove instrumental polarization (leakage-term calibration), and 3C 48 as a polarized reference to calibrate the phase difference between the right-hand and left-hand circular polarization signal path. Note that 3C 84 shows weak $\sim 0.2\%$ linear polarization at 22 GHz (G. B. Taylor et al. 2006), which is small compared to the expected $\sim 3\%$ instrumental polarization. We viewed linear polarizations $\lesssim 0.2\%$ skeptically as they may reflect systematic error by assuming zero polarization for 3C 84. After accounting for pointing overheads and calibrator observations, the total integration time on NGC 1068 was 2.87 hr.

Data reduction broadly followed the approach used for the previous epoch (HSA code BG262J; GI23) with a few extra steps to ensure proper polarization calibration. All calibration steps were performed in AIPS (I. Associated Universities 1999) following the procedures recommended by NRAO. One key step was determining multiband delays to ensure that phase calibration solutions could be transferred from the maser IF to the continuum IFs (AIPS task VLBAMPCL). Unfortunately, the multiband delay solutions failed specifically for the Maunakea antenna, so all baselines to that telescope were discarded (flagged) in the final calibrated data set.

After initial calibration of amplitudes, rates, and delays, we recalibrated phase rates based on the channel containing the brightest H₂O maser, which, for this epoch, had an integrated flux density $S_\nu = 345$ mJy at V (LSRK) = 1369 km s⁻¹. The resulting rate corrections were applied specifically to NGC 1068 and the phase reference J0239–02. This correction introduces an astrometric offset that displaces J0239–02 from its reference position of about 7 mas; this offset is applied in reverse to determine the astrometric positions of the maser spots in the J2000 reference frame. The expected absolute astrometric precision is ~ 0.5 mas, but, because they share a common phase reference, the relative astrometry between the maser spot positions and the 22 GHz continuum is precise, limited mainly by signal to noise (GI23). In this work, all positions are reported or plotted as offsets relative to R.A. (J2000) = 02^h42^m40^s.70907, decl. (J2000) = $-00^{\circ}00'47''.9444$.

Calibrating circular polarization (Stokes V) is challenging as it is calculated from the difference of bright signals in the RR and LL feeds. We adopted a conservative approach and applied an amplitude self-calibration cycle assuming $V=0$ for the brightest maser feature (the Zero- V Self-calibration technique of D. C. Homan & J. F. C. Wardle 1999). If the brightest maser has an intrinsic circular polarization, this self-calibration imposes artificial circular polarization on other maser spots and the continuum. In the end, we did not find credible detections of circular polarization; we conclude that any intrinsic circular polarization is below the detection level, $| \text{Stokes } V | \lesssim 1$ mJy (1σ) (see the discussion in GI23).

2.2. Maser Astrometry and Spectropolarimetry

After primary calibration in AIPS, all imaging tasks were performed in DIFMAP (M. Shepherd 2011). To measure the positions of the maser spots, we used a suitably modified version of `automap`, a script provided with the DIFMAP distribution. The modified script alternates between offset fields associated with radio components S1 and C (the disk and jet masers, respectively) and a control field located midway between the radio components. For maser channels with high signal-to-noise ratios (S/N) in Stokes I , we fit the visibilities with Gaussian surface brightness models; we used point-source models for channels with lower S/N. Imaging was used only to initialize model components and assess residuals; we added model components until the residual peak in the image plane fell below 5σ . To filter false positives, we rejected candidate maser spots whose peak brightness was less than the magnitude of the most negative pixel in the sky plane, and we rejected spots fainter than the brightest pixels in the control field. Finally, we applied a spatial filter to remove false positives associated with sidelobes of the synthetic beam. With natural weighting, the characteristic background rms in the line-free channels is 0.7 mJy beam⁻¹, and the synthetic beam size is 1.34×0.52 mas, PA 4^o.2. For reference, the EVN Calculator predicts an ideal background rms of 0.6 mJy beam⁻¹. In the brightest channel, the peak flux density is 280 mJy beam⁻¹, and the background rms is 1 mJy beam⁻¹; therefore, the measured dynamic range limit is 280:1.

We also generated images in the Q , U , and V Stokes parameters to search for linear and circular polarization. We used point-source models, initialized at the Stokes I positions, to fit the polarized flux. Figure 2 shows the linear polarization images for the brightest five channels in Stokes I . Polarized flux was searched to the limit Stokes $I > 30$ mJy. There were no significant detections on the Stokes V images.

To assess false detections, we applied a linear regression between the Stokes I , Q , and U positions and added a mixture model to identify positional outliers (D. W. Hogg et al. 2010; D. Foreman-Mackey et al. 2013). Polarization candidates having an outlier probability $> 10\%$ were rejected; put another way, we rejected polarization candidates whose best-fit position deviated significantly from the Stokes I position. Finally, to obviate the effects of Ricean bias (J. F. C. Wardle & P. P. Kronberg 1974; N. E. B. Killeen et al. 1986; B.-W. Sohn 2011), we used a Monte Carlo calculation to evaluate the fractional polarization and the electric polarization vector position angle (EVPA). Figure 3 shows a map of the maser spots with significant linear polarization, and their properties are summarized in Table 1.

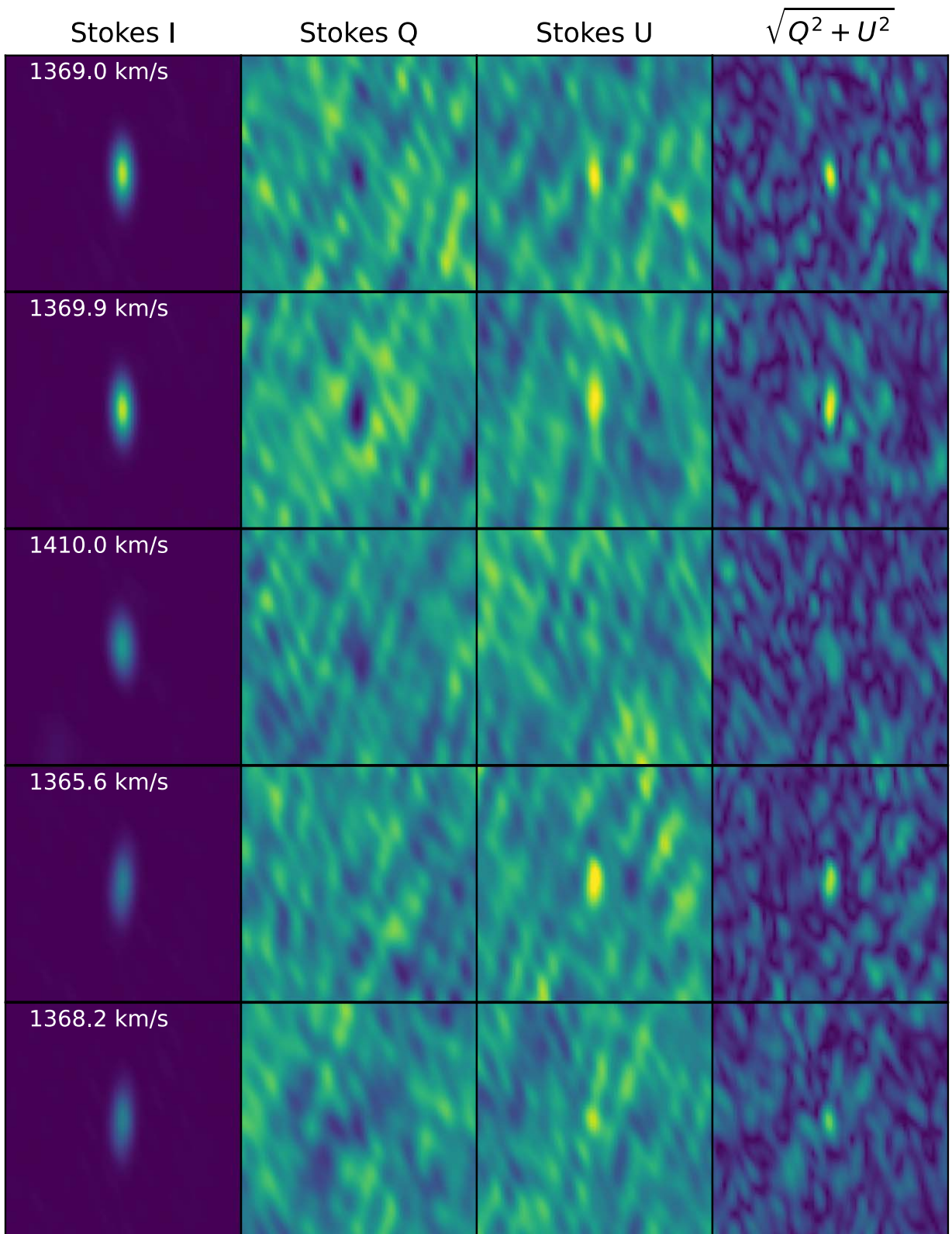


Figure 2. Restored and naturally weighted Stokes I , Q , and U images of the five brightest H₂O maser sources in NGC 1068. The rightmost column shows images of the linearly polarized flux density. Each row is a different spectral channel with recessional velocity, V (LSRK), labeled in the first column. All images are 10 mas and centered on the brightest maser in that channel. The images are displayed with a positive linear stretch in the viridis (blue–green–yellow–white) color map. The display stretches are Stokes I , $(-1, 300)$ mJy beam⁻¹; Stokes Q and U , $(-3, 3)$ mJy beam⁻¹; and polarized flux, $(0, 4)$ mJy beam⁻¹. The synthetic beam size (FWHM) is 1.34×0.52 mas, PA $4^\circ 2$.

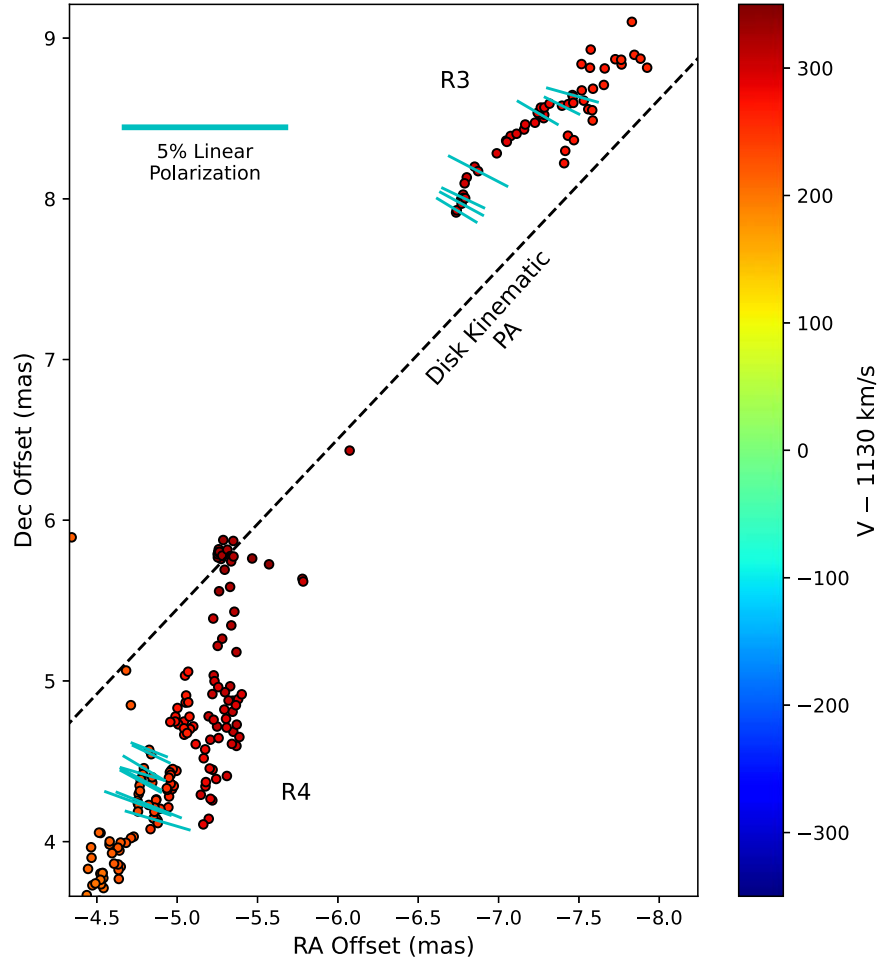


Figure 3. Linear polarization map of the H₂O megamasers of NGC 1068. The maser spots are plotted as in Figure 1, except the spots are now plotted with uniform size. Electric polarization vectors are plotted as cyan lines centered at the position of the peak in the linear polarization maps. The line lengths are proportional to the fractional linear polarization; a 5% linear polarization scale bar is provided at the upper left. Polarization vectors are plotted only for those maser spots where the linear polarization fraction is greater than 5σ . The best-fit disk kinematic PA (GI23), an approximation to the major axis of the edge-on disk, is plotted as a black dashed line. The plot has been modified to help the reader follow the geometry.

Table 1
H₂O Maser Polarization Data

Channel	V (LSRK) (km s ⁻¹)	Stokes I (mJy)	Stokes Q (mJy)	Stokes U (mJy)	f_{pol} (%)	EVPA (deg)	Subgroup	θ_{sg} (deg)
597	1360.5	111 ± 1	-1.8 ± 0.4	1.5 ± 0.4	2.1 ± 0.4	70 ± 6	R4d	88 ± 6
592	1364.8	183 ± 1	-1.4 ± 0.4	2.1 ± 0.4	1.4 ± 0.2	62 ± 6	R4d	80 ± 6
591	1365.6	198.3 ± 0.9	-1.5 ± 0.4	2.3 ± 0.4	1.4 ± 0.2	62 ± 6	R4d	80 ± 6
589	1367.3	188.5 ± 0.9	-2.2 ± 0.4	1.4 ± 0.4	1.4 ± 0.2	74 ± 6	R4d	88 ± 6
588	1368.2	191.2 ± 0.9	-1.3 ± 0.4	2.4 ± 0.4	1.4 ± 0.2	59 ± 6	R4d	77 ± 6
587	1369.0	345.3 ± 0.8	-2.9 ± 0.4	2.7 ± 0.4	1.2 ± 0.1	69 ± 5	R4d	87 ± 5
586	1369.9	345.1 ± 0.8	-2.7 ± 0.4	3.3 ± 0.4	1.2 ± 0.1	65 ± 5	R4d	83 ± 5
583	1372.4	118 ± 1	-1.8 ± 0.4	1.7 ± 0.4	2.1 ± 0.3	68 ± 6	R4c/d ^a	85 ± 7
573	1381.0	99 ± 1	-1.7 ± 0.4	1.0 ± 0.4	2.0 ± 0.4	70 ± 11	R4c	86 ± 11
541	1408.3	130 ± 1	-1.8 ± 0.4	1.0 ± 0.4	1.6 ± 0.3	70 ± 11	R3d	74 ± 11
539	1410.0	228 ± 1	-1.6 ± 0.4	2.1 ± 0.4	1.2 ± 0.2	64 ± 6	R3d	80 ± 6
535	1413.4	189 ± 1	-1.3 ± 0.4	2.3 ± 0.4	1.4 ± 0.2	60 ± 6	R3d	84 ± 6
523	1423.6	105 ± 1	-1.2 ± 0.4	1.7 ± 0.4	2.0 ± 0.4	63 ± 7	R3d	81 ± 7
521	1425.3	162 ± 1	-1.3 ± 0.4	2.0 ± 0.4	1.5 ± 0.2	62 ± 6	R3d	82 ± 6
520	1426.2	148 ± 1	-1.3 ± 0.4	1.6 ± 0.4	1.4 ± 0.3	65 ± 7	R3d	79 ± 7
519	1427.0	171 ± 1	-1.1 ± 0.4	2.1 ± 0.4	1.4 ± 0.2	59 ± 6	R3d	85 ± 6

Notes. Only maser spots with $f_{\text{pol}} > 5\sigma$ significance are included in this table. The subgroup is based on cross identification with maser spots in GI23. The EVPA uncertainty includes a 4° systematic uncertainty added in quadrature to the statistical uncertainty. The PA position angle difference between the subgroup axis and the EVPA, θ_{sg} , is defined as the minimum of the supplementary angles between the two vectors.

^a The subgroup identification for this maser spot is ambiguous. We averaged the properties of subgroups R4c and R4d to calculate θ_{sg} .

All of the polarization detections are associated with the R3d, R4c, and R4d subgroups, as defined in [GI23](#). After outlier rejection, there are 16 maser spots with fractional linear polarizations $f_{\text{pol}} > 5\sigma$ significance. Typical values are $f_{\text{pol}} \sim 1.5\%$.

2.3. Continuum Imaging

We transferred calibration solutions from the maser IF to generate the continuum image and used natural weighting in the Fourier transform. For the image presented in [Figure 1](#), we used a sum of elliptical Gaussian and point-source models to reconstruct the continuum image. Fitting was performed interactively in DIFMAP. We added model components one at a time, elliptical Gaussians for brighter, clearly resolved sources, and point sources for fainter, compact sources. We performed nonlinear model fitting using the DIFMAP task `modelfit`. In all, 50 iterations usually sufficed to minimize χ^2 for a given set of model components. We stopped adding model components when the sidelobes in the residual map were indistinguishable from background noise, $11 \mu\text{Jy beam}^{-1}$, which compares well with that predicted by the [EVN Calculator](#), $12 \mu\text{Jy beam}^{-1}$. Ultimately, the S1 continuum model consisted of six Gaussians and two point sources. The model components were convolved with the restoring beam ($1.46 \times 0.54 \text{ mas}$, PA $1^\circ.5$) and added to the residual image to create the restored image. For reference, the HSA recovers roughly half of the flux density of S1 compared to a recent 22 GHz VLA measurement: the total HSA flux is $7 \pm 1 \text{ mJy}$, compared to $14.7 \pm 0.8 \text{ mJy}$ for the VLA (I. M. Mutie et al. [2024](#)).

3. Results and Discussion

The new continuum image ([Figure 1](#)) is the currently highest-resolution image of the nuclear radio source. It reveals for the first time a compact radio source at the kinematic center of the molecular accretion disk. Following the convention used for the Galactic center (Sgr A'; B. Balick & R. L. Brown [1974](#)) and M 87 (M87'; Event Horizon Telescope Collaboration et al. [2019](#)), we identify this compact source as NGC 1068*. There is resolved radio continuum emission extending roughly 6 mas (0.4 pc) east and west of NGC 1068* along PA $\sim 105^\circ$. This extended feature broadly resembles the morphology observed in 5 and 8.4 GHz continuum (J. F. Gallimore et al. [2004](#)), except for the sharp bends at the extreme eastern and western ends. As this structure is perpendicular to the local outflow axis, we maintain the interpretation that this extended continuum emission arises from plasma in a hot disk located inside the molecular accretion disk (see J. F. Gallimore et al. [1997](#), [2004](#)). There is a $\sim 30^\circ$ rotation in PA between the plasma disk and the maser annulus, suggesting a strong warp at $r \sim 0.5 \text{ pc}$ from the central engine.

Labeled S1-North on [Figure 1](#), we discovered a plume of radio continuum emission north of NGC 1068* that was not resolved at lower frequencies. A hint of this feature is visible in the tapered 22 GHz continuum image of [GI23](#) (see the comparison with the infrared continuum morphology in V. Gámez Rosas et al. [2022](#) and [GI23](#)). As it falls along the direction of the larger-scale radio jet, we speculate that this feature is a cloud of plasma recently ejected from the central engine.

A full kinematic model is beyond the scope of this Letter, but we note that the near-systemic velocity maser spots (the G1 group) closely align with NGC 1068*. Assuming NGC 1068* marks the location of the SMBH, the molecular accretion disk is viewed almost exactly edge on, i.e., inclination $i = 90^\circ$. Our previous model had no constraints on the kinematic center; rather, we sought to minimize the scale height of the disk, resulting in a best fit $i = 75^\circ$ ([GI23](#)). The $\sin i$ correction reduces the inferred SMBH mass by 4%; the revised central mass is now $M = (16.6 \pm 0.1) \times 10^6 M_\odot$, pending a revised model that includes prior constraints on the location of the kinematic center.

All polarization detections are associated with the brighter masers of the R3d, R4c, and R4d maser subgroups. The fractional polarization is typically between 1% and 2%. The 5σ detection limit is about 2 mJy in either Stokes Q or U , so nondetections imply $f_{\text{pol}} \lesssim 1\%$ ($S_I/200 \text{ mJy}$) $^{-1}$, where S_I is the total (Stokes I) flux density. Only 3/754 maser spots have a detection threshold $f_{\text{pol}} \lesssim 1\%$. Therefore, most of the maser spots might have $f_{\text{pol}} \gtrsim 1\%$ but remain undetected in polarized flux owing to limited S/N.

From inspection of [Figure 3](#), the EVPAs appear nearly perpendicular to the local maser filament axes. To quantify the relative orientation, we cross-identified the maser spot positions and velocities against the subgroup properties found in [GI23](#); the subgroup assignments are included in [Table 1](#). The best-fit PAs of the R3d, R4c, and R4d filaments are $-15^\circ.5 \pm 0^\circ.9$, $-18^\circ.1 \pm 0^\circ.3$, and $-36^\circ.5 \pm 0^\circ.5$, respectively ([GI23](#)). We define the PA difference θ_{sg} as the minimum absolute supplementary angle between the EVPA and the PA of the filament; $\theta_{sg} = 0^\circ$ means the EVPA is parallel to the filament, and 90° means perpendicular. All of the measured values of θ_{sg} fall within 3σ of 90° , and none are consistent with $\theta_{sg} = 0^\circ$. In other words, the results are consistent with the EVPAs being perpendicular to the filament axes. With the EVPAs of the maser spots consistently aligned perpendicular to the filaments, Faraday rotation here is likely limited to a few degrees at most.

The relative orderliness of the maser spot EVPAs relative to the filaments they trace indicates a common organizing mechanism: the magnetic field. We assume that the filaments trace the projected orientation of the magnetic field lines, much like solar prominences. Under this assumption, the polarization is perpendicular to the magnetic field lines, indicating that the angles between the sight line and the magnetic field lines are $\theta \gtrsim 55^\circ$ (W. H. T. Vlemmings et al. [2006](#)); in other words, the magnetic field lines lie within 35° of the sky plane. Additionally, it appears that the polarized filaments are not at right angles with the disk plane as was suggested by the deprojection of the inclined disk models of [GI23](#). Since we now have evidence that the disk is viewed edge on and that the magnetic fields are oriented near the plane of the sky, projection effects are small, and the apparent sky rotation of the magnetic field relative to the disk plane is likely close to the true, deprojected rotation. In this case, the filaments are rotated by $\lesssim 30^\circ$ relative to the disk plane (see [Figure 3](#)). R. D. Blandford & D. G. Payne ([1982](#)) demonstrated that a centrifugal outflow results when the poloidal magnetic field falls within 60° of the disk plane. We speculate that this region might be the source of the larger-scale molecular outflow observed with the Atacama Large Millimeter/submillimeter Array (e.g., S. García-Burillo et al. [2014](#); J. F. Gallimore et al. [2016](#); C. M. V. Impellizzeri et al. [2019](#); M. Imanishi et al. [2020](#)). The

filaments are displaced by up to ~ 1 mas (0.07 pc) from the best-fit disk plane (Figure 3), suggesting the masers arise from molecular gas elevated above the edge-on accretion disk. These results are consistent with the proposal of M. Elitzur & I. Shlosman (2006) that such hydromagnetic disk winds might inflate the scale height of dusty molecular gas around the molecular accretion disk, as required by obscuration-based unification schemes.

4. Conclusions

Using the HSA, we have detected linear polarization for the first time in an extragalactic H_2O maser source, the molecular accretion disk of NGC 1068. Furthermore, we have discovered a compact radio source at the kinematic center that we identify as NGC 1068*. We list below the main results and conclusions.

1. The near-systemic masers are nearly aligned with NGC 1068*, indicating that the molecular accretion disk is viewed nearly edge on. This corrects a previous model and slightly reduces the central mass to $M = (16.6 \pm 0.1) \times 10^6 M_\odot$.
2. The maser polarization vectors are perpendicular to their respective maser filaments, arguing for a common polarization mechanism. This result is self-consistent with our proposal that magnetic fields organize the maser filaments.
3. The inferred magnetic fields lie within $\sim 35^\circ$ of the sky plane. Based on the filament morphology, the magnetic fields make an angle of $\lesssim 30^\circ$ with the plane of the molecular accretion disk.
4. The polarization results are consistent with the requirements for a centrifugally directed, hydromagnetic wind. We speculate that this region of the molecular accretion disk might be the source of the larger-scale molecular outflow and potentially elevates molecular gas to create the dust scale height required by obscuration-based unification schemes.

Acknowledgments



We thank Mark Claussen, Amy Mioduszewski, and the staff at NRAO (Socorro) for help setting up the HSA observations. We also thank the anonymous referee for their helpful and constructive review. This Letter makes use of data obtained from the NSF's VLBA and VLA, operated by the National Radio Astronomy Observatory. The National Radio Astronomy Observatory is a facility of the National Science Foundation operated under cooperative agreement by Associated Universities, Inc. The GBT is part of the Green Bank Observatory, which is a facility of the National Science Foundation operated under cooperative agreement by Associated Universities, Inc. J. F.G. and V.H. received travel support from the Tressler Fund for Astronomy at Bucknell University.

Facilities: VLA, GBT, VLBA

Software: AIPS (I. Associated Universities 1999), Astropy (Astropy Collaboration et al. 2013, 2018), DIFMAP (M. Shepherd 2011), emcee (D. Foreman-Mackey et al. 2013).

ORCID iDs

Jack F. Gallimore  <https://orcid.org/0000-0002-6972-2760>
C. M. Violette Impellizzeri  <https://orcid.org/0000-0002-3443-2472>

Samaneh Aghelpasand  <https://orcid.org/0009-0002-1706-7693>
Feng Gao  <https://orcid.org/0000-0002-2581-9114>
Virginia Hostetter  <https://orcid.org/0009-0006-3231-5252>
Boy Lankhaar  <https://orcid.org/0000-0001-8975-9926>

References

- Abramowicz, M. A., & Fragile, P. C. 2013, *LRR*, 16, 1
Anand, G. S., Lee, J. C., Van Dyk, S. D., et al. 2021, *MNRAS*, 501, 3621
Antonucci, R. 1993, *ARA&A*, 31, 473
Associated Universities, I., 1999 AIPS: Astronomical Image Processing System, Astrophysics Source Code Library, ascl:9911.003
Astropy Collaboration, Price-Whelan, A. M., Sipőcz, B. M., et al. 2018, *AJ*, 156, 123
Astropy Collaboration, Robitaille, T. P., Tollerud, E. J., et al. 2013, *A&A*, 558, A33
Balbus, S. A., & Hawley, J. F. 1998, *RvMP*, 70, 1
Balick, B., & Brown, R. L. 1974, *ApJ*, 194, 265
Blandford, R. D., & Payne, D. G. 1982, *MNRAS*, 199, 883
Deguchi, S., Nakai, N., & Barvainis, R. 1995, *AJ*, 109, 507
Deguchi, S., & Watson, W. D. 1986, *ApJ*, 302, 750
Eardley, D. M., & Lightman, A. P. 1975, *ApJ*, 200, 187
Elitzur, M., & Shlosman, I. 2006, *ApJL*, 648, L101
Emmering, R. T., Blandford, R. D., & Shlosman, I. 1992, *ApJ*, 385, 460
Event Horizon Telescope Collaboration, Akiyama, K., Alberdi, A., et al. 2019, *ApJL*, 875, L1
Foreman-Mackey, D., Hogg, D. W., Lang, D., & Goodman, J. 2013, *PASP*, 125, 306
Gallimore, J. F., Baum, S. A., O'Dea, C. P., Brinks, E., & Pedlar, A. 1996, *ApJ*, 462, 740
Gallimore, J. F., Baum, S. A., & O'Dea, C. P. 1997, *Natur*, 388, 852
Gallimore, J. F., Baum, S. A., & O'Dea, C. P. 2004, *ApJ*, 613, 794
Gallimore, J. F., Elitzur, M., Maiolino, R., et al. 2016, *ApJL*, 829, L7
Gallimore, J. F., Henkel, C., Baum, S. A., et al. 2001, *ApJ*, 556, 694
Gallimore, J. F., & Impellizzeri, C. M. V. 2023, *ApJ*, 951, 109
Gámez Rosas, V., Isbell, J. W., Jaffe, W., et al. 2022, *Natur*, 602, 403
Gao, F., Braatz, J. A., Reid, M. J., et al. 2016, *ApJ*, 817, 128
Gao, F., Braatz, J. A., Reid, M. J., et al. 2017, *ApJ*, 834, 52
García-Burillo, S., Combes, F., Usero, A., et al. 2014, *A&A*, 567, A125
Goldreich, P., Keeley, D. A., & Kwan, J. Y. 1973, *ApJ*, 179, 111
Goldreich, P., & Kylafis, N. D. 1981, *ApJL*, 243, L75
Greenhill, L. J., & Gwinn, C. R. 1997, *Ap&SS*, 248, 261
Herrnstein, J. R., Moran, J. M., Greenhill, L. J., Blackman, E. G., & Diamond, P. J. 1998, *ApJ*, 508, 243
Herrnstein, J. R., Moran, J. M., Greenhill, L. J., et al. 1999, *Natur*, 400, 539
Hogg, D. W., Bovy, J., & Lang, D. 2010, arXiv:1008.4686
Homan, D. C., & Wardle, J. F. C. 1999, *AJ*, 118, 1942
Humphreys, E. M. L., Reid, M. J., Moran, J. M., Greenhill, L. J., & Argon, A. L. 2013, *ApJ*, 775, 13
Imanishi, M., Nguyen, D. D., Wada, K., et al. 2020, *ApJ*, 902, 99
Impellizzeri, C. M. V., Gallimore, J. F., Baum, S. A., et al. 2019, *ApJL*, 884, L28
Killeen, N. E. B., Bicknell, G. V., & Ekers, R. D. 1986, *ApJ*, 302, 306
Kuo, C. Y., Braatz, J. A., Condon, J. J., et al. 2011, *ApJ*, 727, 20
Lankhaar, B., Surcis, G., Vlemmings, W., & Impellizzeri, V. 2024, *A&A*, 683, A117
Lankhaar, B., & Teague, R. 2023, *A&A*, 678, A17
Lo, K. Y. 2005, *ARA&A*, 43, 625
Lopez-Rodriguez, E., Packham, C., Jones, T. J., et al. 2015, *MNRAS*, 452, 1902
Modjaz, M., Moran, J. M., Kondratko, P. T., & Greenhill, L. J. 2005, *ApJ*, 626, 104
Mutie, I. M., Williams-Baldwin, D., Beswick, R. J., et al. 2024, *MNRAS*, 527, 11756
Neufeld, D. A., & Maloney, P. R. 1995, *ApJL*, 447, L17
Neufeld, D. A., Maloney, P. R., & Conger, S. 1994, *ApJL*, 436, L127
Ramos Almeida, C., & Ricci, C. 2017, *NatAs*, 1, 679
Shepherd, M., 2011 Difmap: Synthesis Imaging of Visibility Data, Astrophysics Source Code Library, ascl:1103.001
Sohn, B.-W. 2011, *JASS*, 28, 267
Surcis, G., Tarchi, A., & Castangia, P. 2020, *A&A*, 637, A57
Taylor, G. B., Gugliucci, N. E., Fabian, A. C., et al. 2006, *MNRAS*, 368, 1500
Vlemmings, W. H. T., Bignall, H. E., & Diamond, P. J. 2007, *ApJ*, 656, 198
Vlemmings, W. H. T., Diamond, P. J., van Langevelde, H. J., & Torreses, J. M. 2006, *A&A*, 448, 597
Wardle, J. F. C., & Kronberg, P. P. 1974, *ApJ*, 194, 249